General Syntheses of High-performance Thermoelectric Nanostructured Solids without Post-Synthetic Ligand Stripping

Yue Lou [†,┼], *Xiaokun Li* [†,┼], *Zhan Shi* [††], *Hao Zhou, Tianli Feng,* [†††] *Biao Xu* [*,†,¶]

KEYWORDS. Thermoelectric, Colloidal nanocrystals, Ligands, Metallic chalcogenides.

ABSTRACT. Ligand-assisted wet chemical synthesis is a versatile methodology to produce controllable nanocrystals (NCs), which have been applied in many applications ranging from biomedicine to sensing and energy. The selection and post-treatment of ligands play a significant role in the properties of the nanomaterials, and numerous related technologies have been proposed for improving the performance of functional devices. Herein, we demonstrate that retaining ligands can improve the thermoelectric performance of most colloidal-synthesized thermoelectrics nanomaterials (e.g., SnSe, $Cu_{2-x}S$, $AgBiSe_2$, and $Cu_2ZnSnSe_4$), in comparison to the conventional methods that strip ligands using multi-step cumbersome and costly processes. Retained organic ligands on the surface of colloidal NCs are transformed into organic carbon as a secondary phase within the matrices. Various chemical, structural, electrical, and physical characterization of non-stripped and striped (control) samples, combined with theoretical analyses, confirm that the carbon

capping layer slightly affects the electric transport but largely reduces the thermal conductivity. As a result, the materials with ligands retained achieved higher peak and average thermoelectric figure of merits (*zT*) and better mechanical properties. Our method can not only be applied to the materials studied here but is expected to work for all other colloidal thermoelectric NCs, providing great potential for thermoelectrics research and development. It can also be applied to many other fields, such as photocatalysis, electronic devices, and photovoltaics, where the regulation of ligands may significantly enhance performance.

INTRODUCTION.

Colloidal synthesis has shown great potential in many applications, including optoelectronics (solar energy conversion, lighting, display technology), bio-labeling (imaging, detection), catalysis, and thermoelectrics. [1-4] The synthesized colloidal nanocrystals usually consist of inorganic crystalline cores with layers of organic molecule ligands (e.g., oleic acid, trioctylphosphine oxide, alkanethiols, etc.) attached to their surfaces. The choice of ligands is of utmost importance for the colloidal stability and function of NCs and NCs-based devices. The size, chemical composition, structure, and morphology of the nanocrystal cores are regulated by ligands during the nucleation and growth process, determining the physiochemical properties. The interparticle distance, colloidal dispersion, and packing density of an NCs assembly determined by the ligand nature/coverage strongly affect the charge carrier transport properties, thermal conductivity, and chemical reactivity. [5, 7, 8] For example, Robert Y. Wang et al. proposed a novel ligand-crosslinking process to increase the thermal conductivity of NC solids by overcoming the thermal-transport bottleneck between adjacent colloidal NCs. Nanfeng Zheng et al. demonstrated

that the unique ligand system could modify the active sites and improve the catalytic capability of metal PdAu bimetallic nanoclusters catalysts. [6]

For thermoelectric materials, the performance is generally evaluated by the dimensionless figure of merit zT ($zT = S^2\sigma T/\kappa$, where S, σ, T, and κ are the Seebeck coefficient, electrical conductivity, absolute temperature, and thermal conductivity, respectively). [7, 9, 10] A good thermoelectric material requires high power factor ($S^2\sigma$) and low thermal conductivity (κ). An effective strategy to achieve depressed thermal conductivity is to sinter ligand-assisted wet-chemistry-synthesized nanoparticles into dense nanostructured blocks, which provide enhanced scattering of phonons at the numerous grain boundaries. This process leaves organic ligands at the NC surfaces, and it is a common practice to have a pre-process to thermally decompose the organic ligands, chemically remove them, or replace long organic ligands with shorter organic groups or inorganic ligands before sintering. [11-13] For instance, Yu et al. [15] removed organic ligands of large-scale colloidal $Cu_2ZnSnSe_4$ NCs by dealing with hydrazine before NCs consolidation. With this strategy, various materials such as Cu_2SnSe_3, [16] Bi_2Te_3, [17] $Cu_2CdSnSe_4$, [18] and Cu_5FeS_4 [19] were sintered into pellets by spark plasma for thermoelectric applications. Maria Ibáñez et al. [20] removed ligands by heating the nanoparticle powders under inert gas inside a tube furnace before the hot press procedure. In addition, Talapin et al. investigated surface ligand exchange by metallic cation, halide anions, metal chalcogenide, and halide perovskites for NCs-ligand interface modification and optimized thermoelectric performance. [3, 21-23] However, all these pre-sintering (or post-ligand) treatments are multi-step processes, which are cumbersome and costly. [4, 5, 14] Also, they often need expensive hydrazine or thiols, which should be cautiously handled due to their high toxicity and flammability

feature. The interfacial modification without stripping the organic ligands at the NCs surfaces has rarely been studied and remains a challenge.

Herein, an optimal strategy to retain the ligands is proposed, in contrast to the traditional methods that strip the ligands. We demonstrate the thermoelectric properties of SnSe, $Cu_{2-x}S$, $AgBiSe_2$, and $Cu_2ZnSnSe_4$ NCs without removing original long organic ligands. Ligand coatings can be partially retained and used as controllable molecular solders, simultaneously acting as precursors for forming secondary carbonaceous phases during NCs consolidation. Calculations indicate that the introduced high-density carbon-inorganic interfaces provide high thermal boundary resistance, which suppressed the thermal conductivity of the materials. As a result, compared with control samples (with ligands stripping), the samples without ligands stripping show higher peak and average zT values. In addition to excellent TE performance, $Cu_{2-x}S$ without ligand stripping showed improved mechanical properties, which provide great potential for device applications. The novel preparation method without ligands stripping reduces the use of solvents and toxic reagents and enables the cost-effective fabrication of efficient TE materials, which is a practical example of atomic economy and green chemistry.

RESULTS AND DISCUSSION.

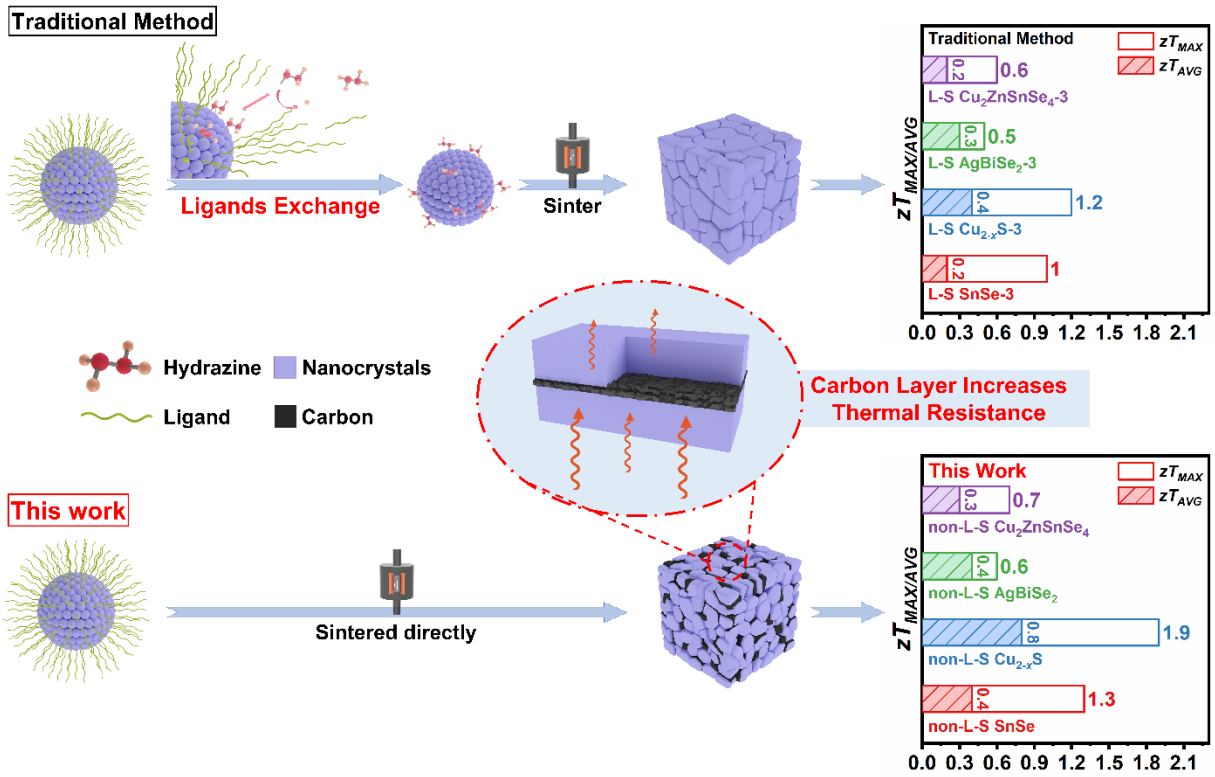

Figure 1. Improving TE performance through retained organic ligands. Schematic diagram of the nanocrystals (SnSe, $Cu_{2-x}S$, $AgBiSe_2$, and $Cu_2ZnSnSe_4$) with/without original long organic ligands stripping.

Figure 1 shows the synthesis processes, comparing the commonly used ligand-stripping method and the new ligand-retaining method. First, the nanoparticles were synthesized by a colloidal synthesis approach, which formed a layer of ligand molecules on the nanoparticle surfaces. Then, depending on whether these nanoparticles were treated by hydrazine to remove ligand molecules or not, the process is named ligand-stripping or ligand-retaining process. After that, the nanoparticles were sintered into dense nanostructured blocks using SPS. As a proof of concept, we selected SnSe (the record-high *zT* thermoelectric material), phonon-liquid electron-crystal $Cu_{2-x}S$, diamond-like structure $AgBiSe_2$, and multinary $Cu_2ZnSnSe_4$ with the commonly used long alkyl

chain organic ligands (oleylamine (OAm), oleic acid (OA), and dodecanethiol (DDT)) as the examples. The sintering and molding of as-synthesized nanocrystals lasted for a short time (30 min) in a closed die during SPS, preventing the volatilization of a large number of ligands. Therefore, the remaining organic ligands thermally decomposed and generated organic carbon as a secondary phase within the matrices, forming the novel inorganic NCs-organic carbon interface (Figure S1). The well-developed surface chemistry of colloidal NCs by retained ligands offers the opportunity to engineer the interfaces and microstructures of the assembled solids, which effectively introduces interfacial resistances and reduces thermal conductivity, resulting in a high average zT and excellent mechanical properties. In contrast, hydrazine as a Brönsted base allows a mild reaction to remove the original capping ligands from the nanocrystal surfaces. Meanwhile, the strong Lewis base N_2H_4 with lone pairs of electrons can saturate dangling bonds at the nanocrystal surface. In addition, N_2H_4 is also a reducing agent, thus producing nonoxidized inorganic NCs. In this study, NCs are treated with hydrazine hydrate 0, 1, and 3 time(s), referred to as non-L-S sample, L-S sample-1, and L-S sample-3, respectively.

The atomic structures of the samples were characterized through several techniques. The representative X-Ray Diffraction (XRD) patterns (Figure S2) demonstrate the crystalline structure of the SnSe, $Cu_{2-x}S$, $AgBiSe_2$, and $Cu_2ZnSnSe_4$ NCs, which are indexed to the orthorhombic *Pnma* phase (JCPDS: 89-0232), tetragonal $P4_32_12$ and monoclinic $P2_1/c$ phase (JCPDS: 29-0578 and 83-1462), hexagonal $P\bar{3}m1$ phase (JCPDS: 29-1441) and cubic $F\bar{4}3m$ phase (JCPDS: 16-0670), respectively. The hydrazine hydrate treatment does not change the crystal structure of the materials. The cell parameters of the above materials are shown in Table S4 in the supporting information. The transmission electron microscopy (TEM) images of the SnSe, $Cu_{2-x}S$, $AgBiSe_2$,

and $Cu_2ZnSnSe_4$ NCs characterize the size distribution and morphology of as-synthesized NCs (Figures 3a and S4). Disk-like, small sphere-like, irregular, and cubic shapes with average sizes of around 336 (± 65) nm, 18 (± 3) nm, 19 (± 4) nm, and 13 (± 2) nm are obtained for these four materials, respectively. The high-resolution TEM (HRTEM) images (Figures 3b and S4) illustrate that the crystal lattice fringes with d-spacing of 0.30 nm, 0.23 nm, 0.31 nm, and 0.20 nm correspond to the reflection of (0 1 -1), (1 -1 0), (0 -1 2), and (0 1 0) planes of SnSe, $Cu_{2-x}S$, $AgBiSe_2$, and $Cu_2ZnSnSe_4$ NCs, indicating the highly crystalline nature of the orthorhombic, tetragonal and monoclinic, cubic, and hexagonal structures.

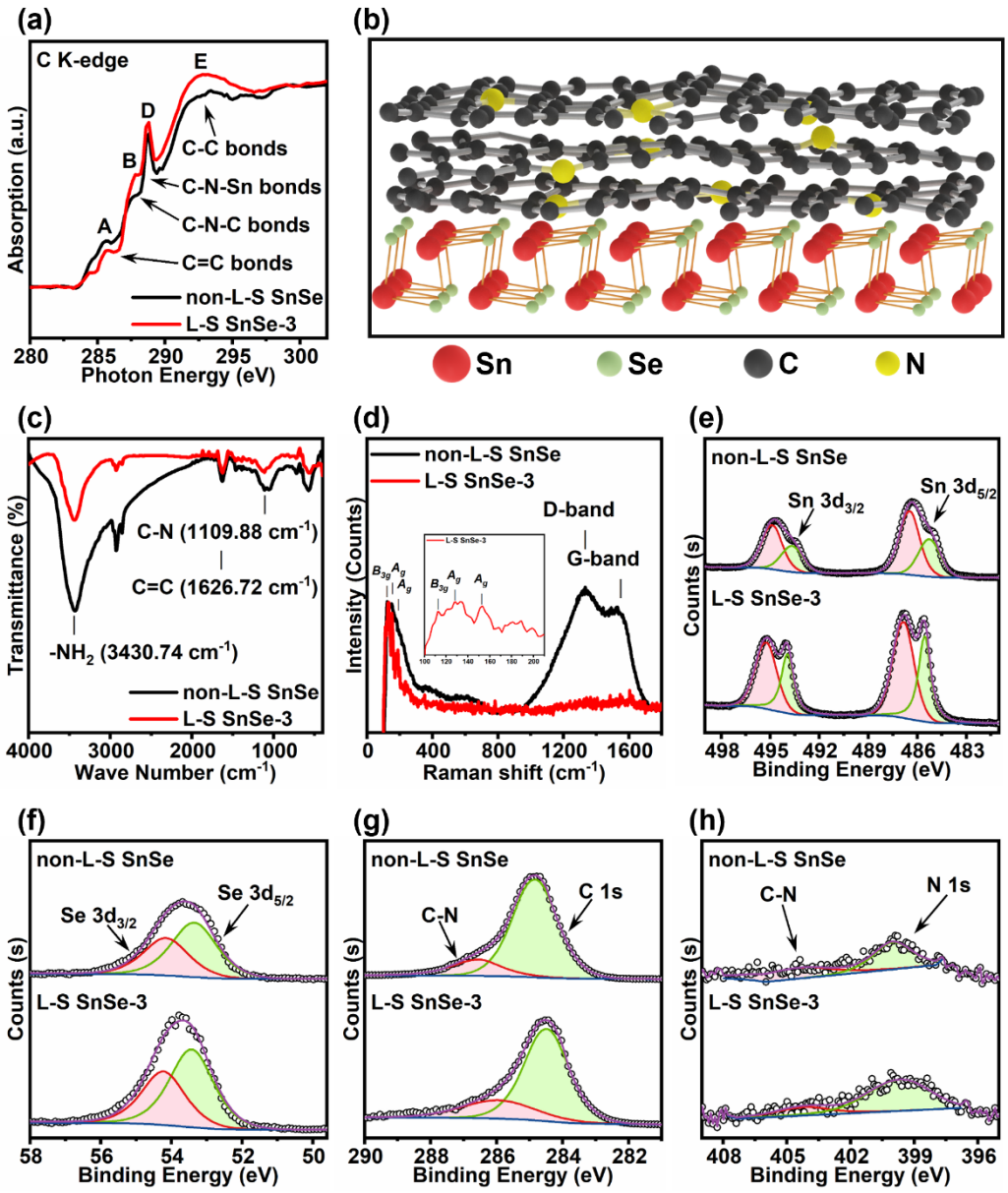

Figure 2. (a) C K-edge soft X-ray absorption near-edge spectroscopy (XANES) normalized spectra, (b) Schematic diagram of NCs surface morphology structure, (c) Fourier transforms infrared (FTIR), and (d) Raman spectra of non-L-S SnSe and L-S SnSe-3. The XPS peak areas of (e) Sn $3d_{3/2}$ and Sn $3d_{5/2}$, (f) Se $3d_{3/2}$ and Se $3d_{5/2}$, (g) C 1s, and (h) N 1s of the non-L-S SnSe and L-S SnSe-3.

To identify the chemistry of the organic surfactant shell surrounding the thermoelectric materials before and after ligand stripping, we performed Fourier transforms infrared (FTIR) spectroscopy characterization for dried samples. As shown in Figure 2c, the presence of the OAm molecules is identified by the symmetric and asymmetric stretching vibrations of -NH_2 at 3430.74 cm^{-1}, the bending vibrations of C=C bonds at 1626.72 cm^{-1}, and the bending vibration of the C-N bond at 1109.88 cm^{-1}. These features are lighter in the L-S SnSe-3 sample, compared with the original non-stripped samples. The L-S SnSe-3 sample also shows a ligand exchange by hydrazine at the surface of colloidal nanoparticles. This result is in good accordance with Raman spectra (Figure S3), in which the carbon peaks of the samples were calibrated relatively to the charateristic B_{3g} and A_g Raman modes of SnSe at 109 cm^{-1}, 128.5 cm^{-1}, and 150 cm^{-1}. [24, 25] Two dominant carbon peaks of SPSed SnSe samples without ligand stripping at around 1334 and 1526 cm^{-1} correspond to the D and G bands, respectively (Figure 2d). The D band is assigned to the breathing mode of A_{1g} symmetry or sp^3-rich phase for the disordered graphite. The G band corresponds to the E_{2g} mode of 2D graphite, which is related to the vibration of sp^2-hybridized carbon. The D and G bands indicate that the surface ligands were turned into organic carbons during the sintering process. The relatively high intensity of the D-band and G-band (I_D/I_G) (1.11) for SPSed non-L-S SnSe indicate a high degree of disorder of carbon, which is beneficial for enhancing phonon scattering and reducing thermal conductivity. For SPSed L-S SnSe-3, the intensity of the D and G bands are significantly decreased due to the ligand stripping and the elimination of carbon during the annealing process. [26, 27, 33] This is also proved by the content analysis by carbon and sulfur automatic analyze. The carbon content (1.23 wt%) for SPSed non-L-S SnSe pellets was much higher than that (0.264 wt%) of L-S SnSe-3 pellets.

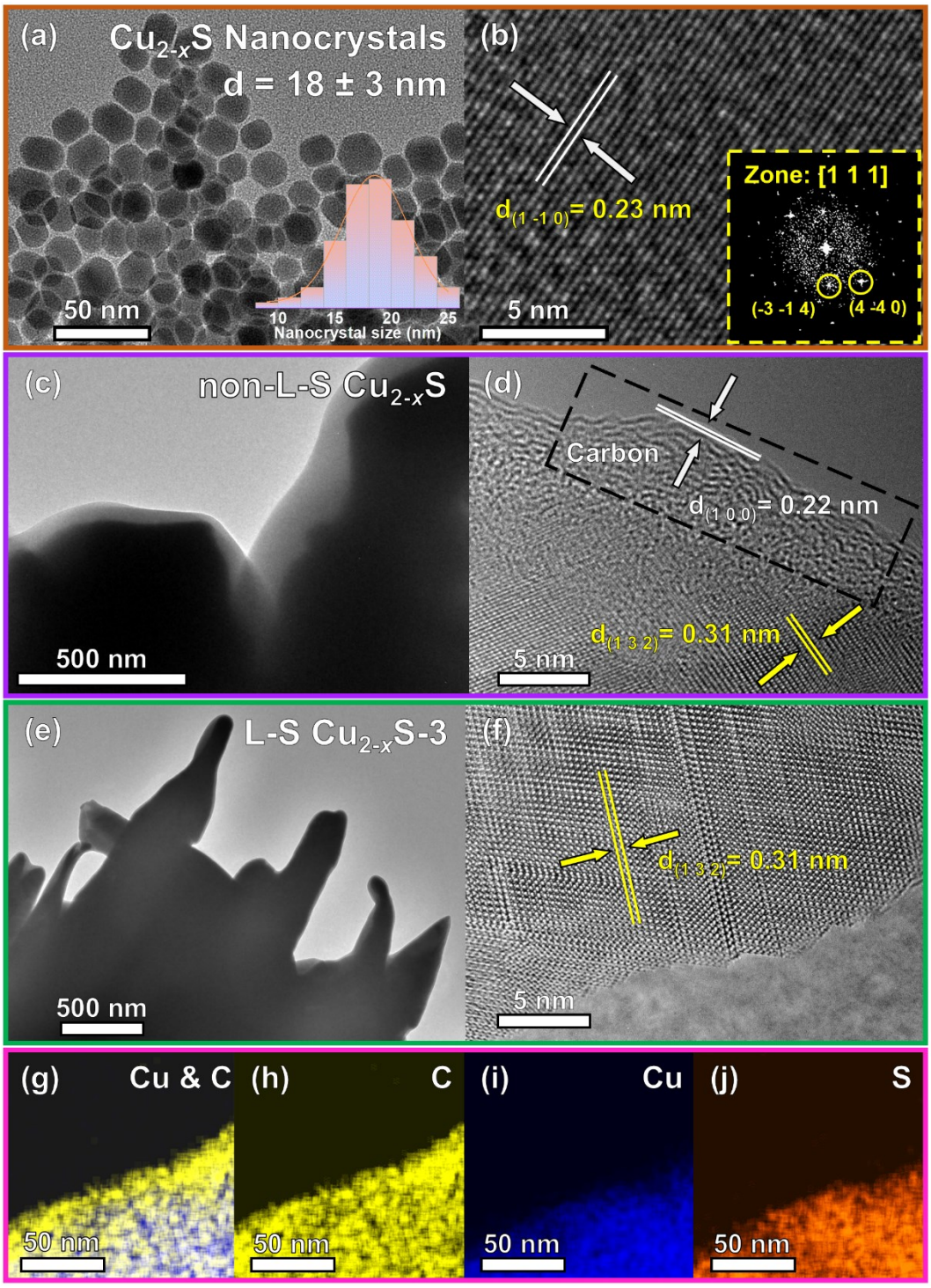

Figure 3. Morphology characterizations of $Cu_{2-x}S$ samples. (a, b) TEM and HRTEM images of the as-synthesized small sphere-like $Cu_{2-x}S$ nanoparticles, insert: the FFT pattern. (c, d) TEM and HRTEM images of the non-L-S $Cu_{2-x}S$ sample, the carbon is marked in the black dashed box, (e,

f) TEM and HRTEM images of the L-S $Cu_{2-x}S$-3. (g-j) The energy dispersive spectroscopy (EDS) elemental mapping of C (yellow), Cu (blue), and S (orange) for non-L-S $Cu_{2-x}S$ particles.

As presented in Figure 3c, TEM images treated with ion thinning demonstrate that the $Cu_{2-x}S$ NCs are embedded in the nanostructured solids, and the ligands are carbonized as a carbon coating on the grain of $Cu_{2-x}S$. HRTEM images prove the high crystallinity of $Cu_{2-x}S$ NCs and the formation of NCs-carbon interfaces after annealing (Figure 3d). The carbon is mainly distributed along with the marginal area of Cu and S elements, as depicted in the EDS elemental mapping in Figures 3g-j. All elements in the samples show homogeneous distributions. The carbon coating of $Cu_{2-x}S$ with ligands striping is rarely observed (Figure 3e), consistent with the FTIR, Raman, and carbon content analysis results discussed above. In addition, elemental mappings were performed to identify Sn, Se, Ag, Bi, Cu, and Zn elements in nanoparticles for SPSed SnSe, SPSed $AgBiSe_2$, and SPSed $Cu_2ZnSnSe_4$ (Figures S6-S8).

Thermoelectric properties

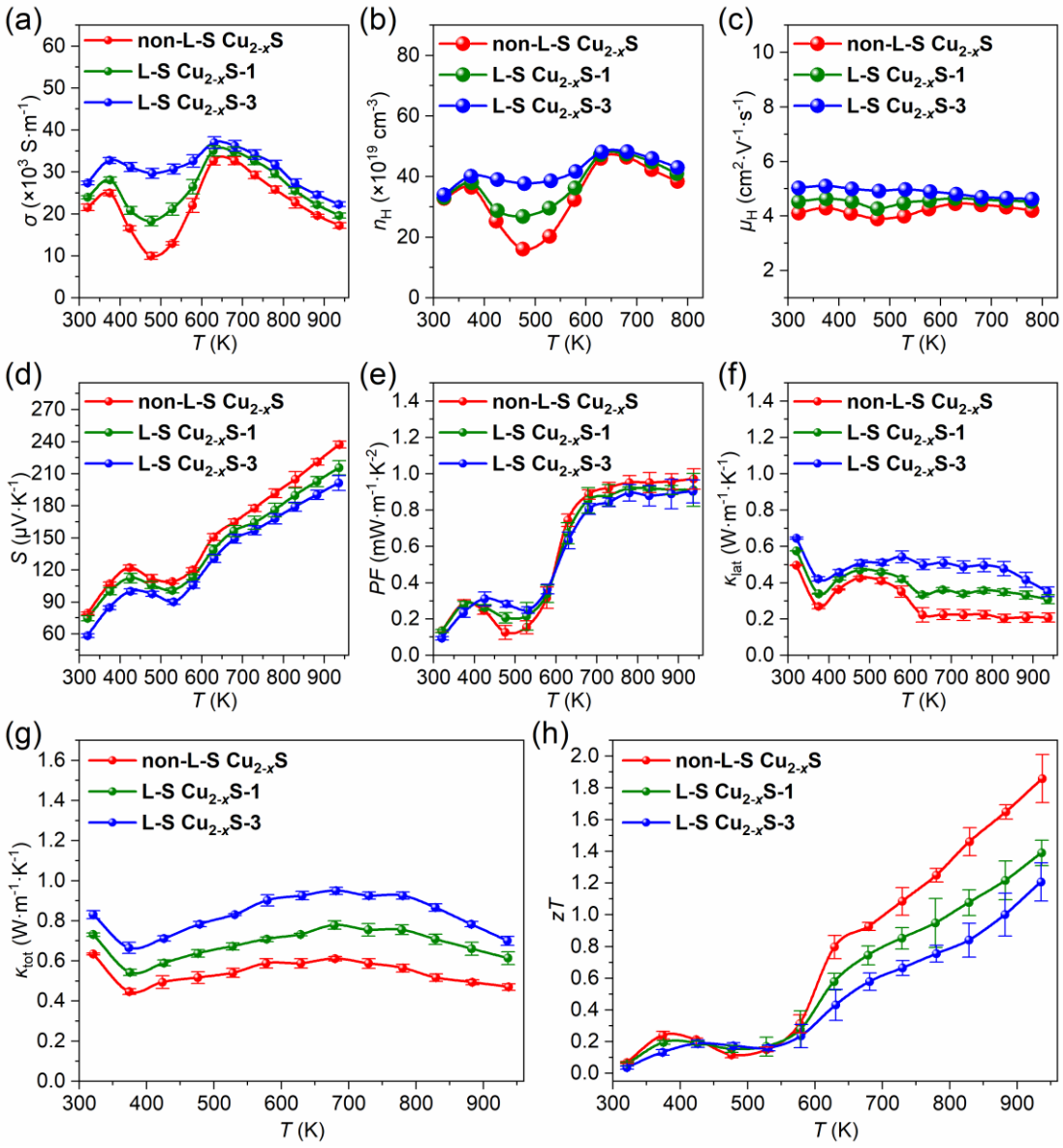

Figure 4. Thermoelectric properties of the non-L-S $Cu_{2-x}S$, L-S $Cu_{2-x}S$-1, and L-S $Cu_{2-x}S$-3 samples: Temperature-dependent (a) electrical conductivity (σ), (b) carrier concentration (n_H), (c) carrier mobility (μ_H), (d) Seebeck coefficient (S), (e) power factor (PF), (f) lattice thermal conductivity (κ_{lat}), (g) total thermal conductivity (κ_{tot}), and (h) zT.

The thermoelectric properties were measured in the temperature range from 300 K to 937 K, with σ, n_H, μ_H, S, κ, and zT of $Cu_{2-x}S$ shown in Figure 4, and those of SnSe, $AgBiSe_2$, and $Cu_2ZnSnSe_4$ are shown in Figures S10, S11, and S12, respectively. The L-S and non-L-S samples show similar temperature dependences of the transport properties. For $Cu_{2-x}S$, the electrical conductivity shows two peaks because of the phase transition, which is similar to the reports in the literature. For non- L-S $Cu_{2-x}S$, the two peaks are 21.5×10^3 S m^{-1} and 32.2×10^3 S m^{-1}at 323 K and 650 K, respectively. The stripping of the organic ligands increased the electrical conductivity for all four materials, likely due to the reduced carrier scattering by nanoscale grain boundary and reduced carbon interfaces.

The further understand the electrical transport properties change after ligands stripping, we analyze another chemical change induced by hydrazine (which stripped ligands). Hydrazine with lone pairs of electrons can replace ligands by saturating dangling bonds. Therefore, hydrazine hydrate leads to more nitrogen doping in nanostructured solids, in which the N doping reconstructs the remaining carbon atoms, resulting in increased defects and carbon disorder. Soft X-ray absorption near-edge structure (XANES) measurements are used to detect the K-edge excitation of elemental C (Figure 2a) to investigate the electronic structure and the nature of the carbon defect of the SnSe-Carbon sample. Four peaks at ~285.5, 287.8, 288.7, and 292.1 eV are denoted as A, B, D, and E, respectively. The absorption peak A corresponds to π* excitations of C=C bonds at the defect sites [28], and the peak E corresponds to the σ* structure of C-C bonds. [29] The strong π* and σ* bands structures show that the carbon is graphitized [30]. In addition, the weak shoulder peaks B and D exist between π* and σ* features, ascribed to the π* excitation of C-N-C bonds in the g-C_3N_4 structure and C-N-Sn bridging bonds, respectively. [28-30] The L-S SnSe-3 has weaker peak A and stronger peak E than the non-L-S SnSe, indicating the elimination of C=C or sp^2-bonding.

Meanwhile, the intensities of B and D features (which are considered as contributions from C-N hybrid bonds of the pyrrole rings) increased after ligands stripping, demonstrating a stronger interfacial interaction between N-doped carbon and SnSe nanoparticles and the defective characteristics of the carbon layer.

The bonding of C-N-Sn, which can transfer electrons from Sn C sites in L-S SnSe-3 materials, can improve electrical conductivity, which is another reason that ligand stripping (hydrazine treatment) can enhance σ. [33] This phenomenon is proved by XPS analysis (Figures 2e-h). In the non-L-S SnSe, the Sn $3d_{5/2}$ peak and Sn $3d_{3/2}$ signal can be deconvoluted into four peaks with binding energies (BE) of 486.4 eV (Sn^{4+}), 494.8 eV (Sn^{4+}), 485.2 eV (Sn^{2+}) and 493.6 eV (Sn^{2+}). Se 3d spectra of non-L-S SnSe can be ascribed to Se $3d_{5/2}$ and Se $3d_{3/2}$ at 53.4 eV and 54.1eV, corresponding to Se^{2-} (Figure 2f). The Sn peaks of L-S SnSe-3 were slightly shifted to high BE compared to non-L-S SnSe (~0.33 eV), implying that the Sn atoms contributed electrons to carbon. The same phenomenon has also occurred in the Se 3d spectra, shifting about 0.12 eV to higher BE. The above results demonstrated a typical electron transfer phenomenon of hybrid materials from SnSe nanoparticles to carbon in SnSe nanostructured solids. [31-33] To investigate the bonding state of nitrogen and carbon, the N 1s and the C 1s spectra are analyzed. The N content is 3.0% for non-L-S SnSe, lower than the 4.2% for L-S SnSe-3, demonstrating a more N doping of the carbon layer in nanostructured solids if hydrazine treatment is adopted. The fitting result of the N 1s peak shows that two peaks at 400.5 eV and 404.2 eV correspond to Pyridinic-N and graphitic-N, and Pyridinic-N is the dominant species. [29-31] The C 1s spectrum can be divided into two peaks at 284.8 eV and higher binding energies of 286.6 eV, corresponding to the sp^2 hybridized graphitic carbon and C-N species. [34]

S decreases with increasing ligand stripping (hydrazine treatment) throughout the entire temperature. For example, as shown in Figure 4d, the room-temperature *S* for the non-L-S $Cu_{2-x}S$, L-S $Cu_{2-x}S$-1, and L-S $Cu_{2-x}S$-3 samples are 79.1, 74.5, and 58.3 $\mu V \cdot K^{-1}$, respectively. Such change is largely related to charging carrier concentration (Figure 4b), which is derived from the material composition. The alkaline hydrazine hydrate treatment often leads to the etching of the surface of NCs and the generation of metal vacancies to increase their carrier concentration. Based on the positive *S* values, all the samples are determined as p-type, likely due to the Cu^+ vacancies in $Cu_{2-x}S$ NCs. The power factors ($PF=\sigma S^2$) of all the samples are shown in Figure 4e. At 937 K, the *PF* of non-L-S $Cu_{2-x}S$ (0.97 mW m^{-1} K^{-2}) is higher than that of the L-S samples (0.90 mW m^{-1} K^{-2}).

Retaining ligands can significantly reduce the thermal conductivity of $Cu_{2-x}S$. The thermal conductivity κ_{tot} (Figure 4g) of the non-L-S $Cu_{2-x}S$ pellet is 0.63 Wm^{-1} K^{-1} at 323 K, which is lower than those of L-S $Cu_{2-x}S$-1 (0.73 $Wm^{-1}K^{-1}$) and L-S $Cu_{2-x}S$-3 (0.83 $Wm^{-1}K^{-1}$). According to the Wiedemann-Franz law, the electronic thermal conductivity can be calculated via $\kappa_{ele} = L\sigma T$, where $L = (1.5 + \exp(-|S|/116)) \times 10^{-8}$) is the Lorenz number. After subtracting κ_{ele} from κ_{tot}, we obtained the lattice thermal conductivity κ_{lat}, as shown in Figure 4f.[9, 35] It is found that the κ_{lat} decreased by as much as 43 % (from 0.35 to 0.20 $Wm^{-1}K^{-1}$) after retaining the ligands.

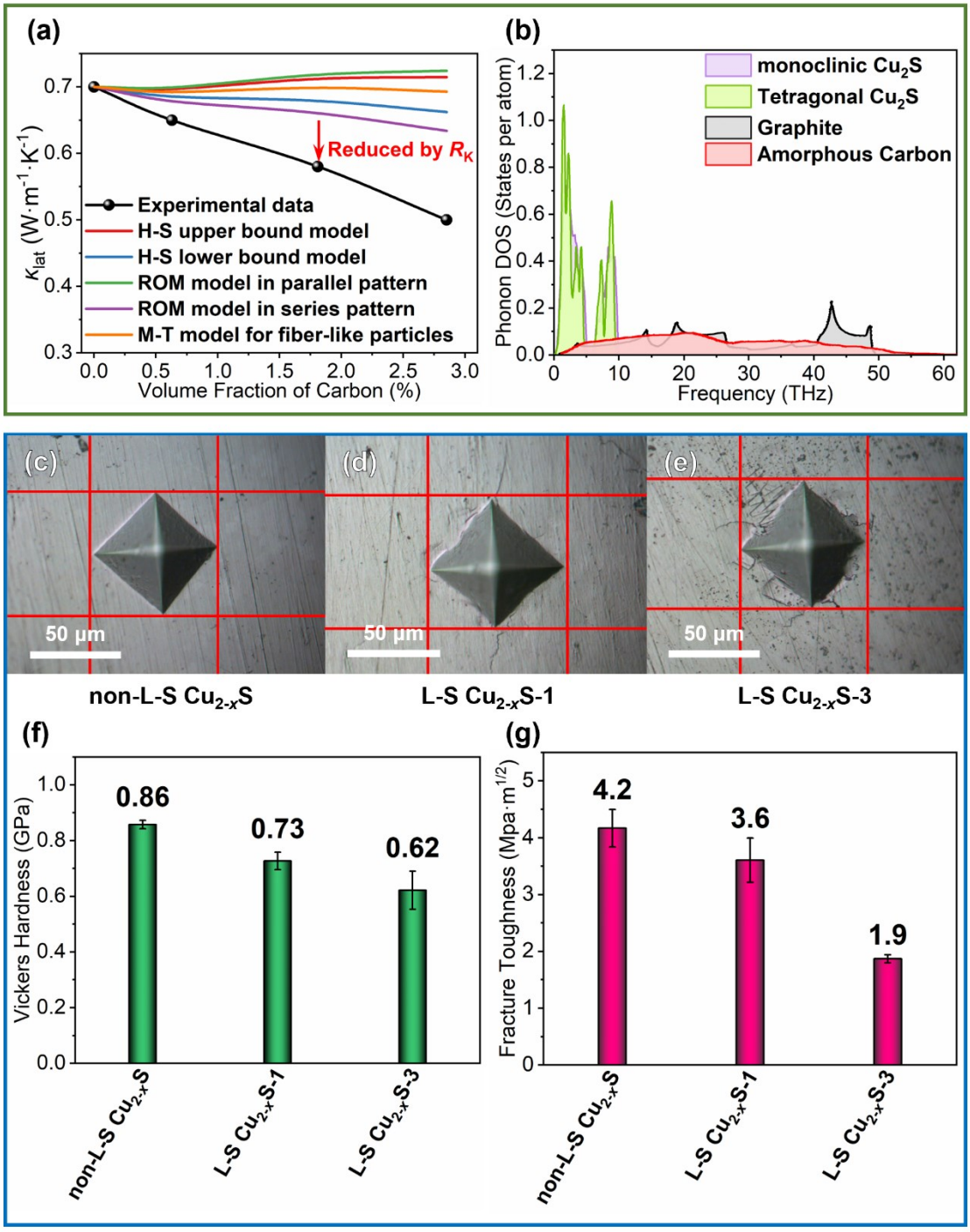

Figure 5. (a) Lattice thermal conductivity (κ_{lat}) at 323K with different contents of amorphous carbon. The thermal conductivities are predicted by the Hashin-Shtrikman bound model (H-S ub and H-S lb), rule of mixture (ROM) model in parallel and series patterns, and Mori-Tanaka (M-T)

model for fiber-like particles. (b) The mismatch in phonon density of states between Cu_2S and different forms of carbon. [36, 37] The microscopic appearance of indentation of the (c) non-L-S $Cu_{2-x}S$, (d) L-S $Cu_{2-x}S$-1, and (e) L-S $Cu_{2-x}S$-3. (f) Micro Vickers hardness and (g) fracture toughness of the non-L-S $Cu_{2-x}S$, L-S $Cu_{2-x}S$-1, and L-S $Cu_{2-x}S$-3.

To understand the decreased lattice thermal conductivity with retaining ligands (or increasing amorphous carbon content) in $Cu_{2-x}S$, we conducted theoretical analyses. First, it is necessary to examine whether it is related to the nanoscale size effect (or phonon scattering by grain boundaries), for which we need to estimate the phonon mean free path (MFP) in $Cu_{2-x}S$ and compare it with the grain size. Therefore, we calculated the phonon dispersion relation, phonon group velocity, and phonon specific heat from first principles using density functional theory (DFT) by Vienna Ab initio Simulation Package (VASP). Using Boltzmann transport equation (BTE, see the supplemental information), if all phonons MFP is assumed to be 1 nm, the thermal conductivity is calculated as 0.14 $Wm^{-1}K^{-1}$ per 1 nm MFP for monoclinic Cu_2S and 0.44 $Wm^{-1}K^{-1}$ per 1 nm MFP for orthorhombic Cu_2S (Table S1). Since the thermal conductivity of the experimental Cu_2S samples varies from 0.2 to 0.6 $Wm^{-1}K^{-1}$, the effective MFP of these samples should be (0.2 - 0.6 $Wm^{-1}K^{-1}$) / (0.14 - 0.44 $Wm^{-1}K^{-1}nm^{-1}$) = 0.5 - 4 nm, which is much smaller than the grain size of 280 ~ 300 nm. Therefore, the reasoning of phonon grain boundary scattering can be excluded.

Since there is no phonon-grain boundary scattering or nanoscale ballistic phonon transport effect, it is safe to use the effective medium approximation (EMA) to model thermal transport. For that, the intrinsic thermal conductivity values of Cu_2S and amorphous carbon are needed. The thermal conductivity of Cu_2S should be approximately 0.7 ~ 0.8 W $m^{-1}K^{-1}$ based on the reference results, and 0.7 $Wm^{-1}K^{-1}$ is adopted here. [38] For amorphous carbon, the thermal conductivity is

quite tricky, varying from 0.2 to 2.2 $Wm^{-1}K^{-1}$, [39] so its upper and lower-limit values are both employed in the calculation. Several classical EMA models for effective thermal conductivity of mixtures were utilized, including the parallel and series models, Hashin-Shtrikman (H-S) bounds model, and the Mori-Tanaka model. All the other EMA models such as Russell, Maxwell and Bruggeman models fall between parallel and series models, which are the hard theoretical upper and lower limits of binary mixture. For detailed information of the EMA models, see the Supporting Information. Figure 5a compares the prediction of effective κ_{lat} by those models with experimental data. We find that EMA models cannot fully explain the low κ_{lat} of Cu_2S composite materials mixed with amorphous carbon. One possible reason is that the EMA models do not consider the interfacial thermal resistances between matrix and fillers (the two phases of a binary mixture). Interfacial thermal resistance (R_K) can be defined as the ratio of the temperature discontinuity to the heat flux at the interface, which generally exists in composite materials because of their large difference in physical properties on the two sides of the interface. Herein, huge dissimilarity in density, sound velocity, and phonon density of states between carbon and Cu_2S matrix can result in a strong scattering of phonons at the composite interfaces, leading to a significant R_K, which can remarkably impede heat conduction.

To estimate the R_K between Cu_2S and amorphous carbon, we calculated phonon density of states (DOS) of Cu_2S by DFT and collected the phonon DOS of different forms of carbon, as shown in Figure 5b. It is found that they exhibits a great mismatch: Cu_2S has extremely high DOS below 10 THz, where the DOS of carbon is minimal, indicating that R_K should be very large. To estimate whether R_K can play a role in reducing the thermal conductivity of Cu_2S, we estimated R_K using the diffusive mismatch model (DMM).[40] R_K is inversely proportional to the phonon transmission coefficient ($\tau_{1\rightarrow2}$), which can be expressed as

$$\tau_{1\to2}(\omega) = \frac{I_1(\omega)}{I_1(\omega)+I_2(\omega)} \quad (1)$$

where

$$I_j(\xi) = \sum_p \iint_{\mathbf{k}:\omega(\mathbf{k})=\xi} \frac{\left[v_g^j(\mathbf{k},p)\hat{n}\right]}{\left\|v_g^j(\mathbf{k},p)\right\|} d\mathbf{S}_{\mathbf{k},p} \quad (2)$$

where **k** is phonon wave vector, ω is the phonon frequency, v_g is the group velocity, $\hat{n}$ the unit normal to the interface plane, p is phonon polarization, and j represents one material. The thermal interface conductance can be calculated with the phonon transmission coefficient $\tau_{1\to2}$ (see the Supporting Information) and then converted into R_K. Moreover, the κ_{lat} can be deduced as follows:

$$\kappa_{\text{lat}} = \frac{\kappa_{\text{grain}}}{1+\frac{2R_K\cdot\kappa_{\text{grain}}}{L}} \quad (3)$$

where L is the grain size and κ_{grain} is the thermal conductivity of Cu_2S matrix grain. If $2R_K\kappa_{grain}/L$ is comparable to or larger than 1, the interfacial thermal resistance is comparable to larger than the thermal resistance of Cu_2S matrix grain. The calculation results (Table S3) show that $2R_K\kappa_{grain}/L$ varies from 0. 24 to 4.10 for different forms of carbon, which indicates that R_K, caused by a large mismatch of phonon DOS for Cu_2S matrix and carbon, plays a significant role in reducing κ_{lat} of Cu_2S composite.

In addition to these factors, residual strains may also reduce the thermal conductivity. To visualize the strain distribution caused by the substantial mismatch of atomic radius, geometric phase analysis (GPA) was performed. According to the GPA strain analysis maps of the strain component parallel to the interface (ε_{xx}) of the SPSed non-L-S $Cu_{2-x}S$ (Figure S9b) and SPSed L-

S $Cu_{2-x}S$-3 (Figure S9d), substantial strain distribution fluctuations of two samples demonstrate retained ligands less affect dislocations at the phase interface.

Owing to the reduced thermal conductivity and the increased power factor, higher zT values of non-L-S $Cu_{2-x}S$ are achieved as 1.9 at 937 K, which is 1.6-fold of the value obtained by L-S $Cu_{2-x}S$-3 (zT = 1.2), indicating our strategy of retaining organic ligands have a significant effect on improving thermoelectric performance (Figure 4f). To validate the vast potential of the described procedure to prepare nanomaterials with enhanced performance, in addition to $Cu_{2-x}S$, we obtained the thermoelectric properties of SnSe, $AgBiSe_2$, and $Cu_2ZnSnSe_4$ pellets, shown in the supplemental information Figures S10-S12. The zT values of the above non-L-S samples prepared by the retained ligands route are higher or comparable to those of L-S sample-3 due to reduced κ_{tot} without severe deterioration of the electrical transport performance. As shown in Figure 1, the highest zT for the L-S SnSe-3, L-S $Cu_{2-x}S$-3, L-S $AgBiSe_2$-3, and L-S $Cu_2ZnSnSe_4$-3 are 1, 1.2, 0.5, and 0.6, respectively, while the highest zT for non-L-S samples are 1.3, 1.9, 0.6, and 0.7, respectively, and the average zT have a similar trend. The surface-ligand influence on properties is related to the effect of surface treatment on the final surface composition and structure. Firstly, the inorganic NCs-organic carbon interfaces effectively scatter long mean-free-path electrons and phonons, which is beneficial to reducing the κ. Under certain conditions, ligands also play an important role in enhancing the S. However, the carbon-nano grain interfaces usually decrease the σ due to the insulating capping layer of carbon. Therefore, improvement of the zT requires that the proportional reduction in electronic carrier mobility (Figure 4c) resulting from increased interfacial scattering is less than the corresponding reduction in thermal conductivity. Balancing the electronic and thermal properties of the interfaces through regulating the amount of retained organic ligands is critical to tailoring material for optimal thermoelectric performance.

After we achieved a record high zT value in the non-L-S $Cu_{2-x}S$, we also evaluated the fracture toughness to understand the effect of retained ligands on the mechanical properties of the $Cu_{2-x}S$ system during sintering. The Vickers hardness (H_v) and fracture toughness (K_{IC}) are measured on the polished surface according to the equations $H_v = 1854.4 \cdot F/D^2$ and $K_{IC} = A \cdot (E/H_v)^{0.5} \cdot (F/c^{1.5})$, where F (in newtons) is the applied load, D (in micrometers) is the length of the diagonal of the resultant impression, the calibration constant is a value of 0.01,[41, 42] c (in micrometers) is the radial crack length of Vickers indentation, and E is Young's modulus of the $Cu_{2-x}S$ samples.[43] We use nanoindentation to measure Young's modulus. Figures 5f and 5g show that the hardness and the fracture toughness of L-S $Cu_{2-x}S$-3 are about 0.62 GPa and 1.9 $MPa \cdot m^{1/2}$, respectively. In contrast, the hardness and fracture toughness of the non-L-S $Cu_{2-x}S$ can reach as high as 0.86 GPa and 4.2 $MPa \cdot m^{1/2}$. Ligands used as controllable molecular solders can generate a bridging effect between $Cu_{2-x}S$ grains and improve their stronger interaction, resulting in optimized mechanical durability.

Conclusion

In conclusion, we report the colloidal synthesis of monodisperse SnSe, $Cu_{2-x}S$, $AgBiSe_2$, and $Cu_2ZnSnSe_4$ NCs. Ligand regulation is used to modulate surface energy, interface structures of nanostructured solids, and introduce controlled amounts of secondary carbon phases. As a result, NCs incorporating a small amount of carbon can decrease κ, maintain a high PF, and increase zT. The procedure promotes the bottom-up assembly of colloidal nanoparticles as a suitable approach to producing efficient thermoelectric materials and provides new insights into improving their

thermoelectric performance. In addition to the high TE performance, the superior mechanical properties of NC-based materials with ligand retention offer great potential for device applications.

Acknowledgments

B.X. thanks financial support from "the Fundamental Research Funds for the Central Universities", No. 30922010201, and the Key Laboratory for Soft Chemistry and Functional Materials of the Ministry of Education, Nanjing University of Science and Technology. Y.L. thanks for financial support from the Jiangsu Provincial Innovation and Entrepreneurship Doctor Program (JSSCBS20210215). H.Z. and T.F. thank the support from National Science Foundation (NSF Award No. 2212830). The calculation used the NSF Extreme Science and Engineering Discovery Environment (XSEDE). This research also used resources of the National Energy Research Scientific Computing Center, a DOE Office of Science User Facility supported by the Office of Science of the U.S. Department of Energy under Contract No. DE-AC02-05CH11231 using NERSC award BES-ERCAP0022132. The support and resources from the Center for High-Performance Computing at the University of Utah are gratefully acknowledged.

ASSOCIATED CONTENT

Supporting Information.

The following files are available free of charge at

Details of experimental section, density functional theory calculation (Table S1-S3), additional X-ray diffraction patterns (Figure S2), additional transmission electron microscopy, and scanning

electron microscopy analyses (Figures S4-S9), and thermoelectric properties of SnSe, $AgBiSe_2$, and $Cu_2ZnSnSe_4$ (Figures S10-S12). (PDF)

AUTHOR INFORMATION

Corresponding Author

Biao Xu - *School of Chemistry and Chemical Engineering, Nanjing University of Science and Technology, Nanjing, 210094, P. R. China* and *Chemical Engineering, Collaborative Innovation Center of Advanced Microstructures, Nanjing University, Nanjing, 210093, P. R. China*; orcid.org/0000-0002-6645-3905; Email: xubiao@njust.edu.cn

Author

Yue Lou - *School of Chemistry and Chemical Engineering, Nanjing University of Science and Technology, Nanjing, 210094, P. R. China;* orcid.org/0000-0002-0364-6582; Email: louyue@njust.edu.cn

Xiaokun Li - *School of Chemistry and Chemical Engineering, Nanjing University of Science and Technology, Nanjing, 210094, P. R. China;* orcid.org/0000-0002-0342-594X; Email: lixiaokun@njust.edu.cn

Zhan Shi - *State Key Laboratory of Inorganic Synthesis and Preparative Chemistry, College of Chemistry, Jilin University, Changchun, 130012, P. R. China;* orcid.org/0000-0001-9717-1487; Email: zshi@mail.jlu.edu.cn

Hao Zhou - *Department of Mechanical Engineering, The University of Utah Salt Lake City, UT 84112 (USA);* orcid.org/0000-0001-6499-1921; Email: hao.zhou@utah.edu.

Tianli Feng - *Department of Mechanical Engineering, The University of Utah Salt Lake City, UT 84112 (USA);* orcid.org/0000-0002-7284-5657; Email: tianli.feng@utah.edu.

Author Contributions

† Y. L. and X.K. L. contributed equally.

Notes

The authors declare no competing financial interest.

REFERENCES

(1) Coughlan, C.; Ibanez, M.; Dobrozhan, O.; Singh, A.; Cabot, A.; Ryan, K. M. Compound Copper Chalcogenide Nanocrystals. *Chem. Rev.* **2017**, *117*, 5865-6109.

(2) Kovalenko, M. V.; Manna, L.; Cabot, A.; Hens, Z.; Talapin, D. V.; Kagan, C. R.; Klimov, V. I.; Rogach, A. L.; Reiss, P.; Milliron, D. J.; et al. Prospects of Nanoscience with Nanocrystals. *ACS Nano* **2015**, *9*, 1012-1057.

(3) Kovalenko, M. V.; Scheele, M.; Talapin, D. V. Colloidal Nanocrystals with Molecular Metal Chalcogenide Surface Ligands. *Science* **2009**, *324*, 1417.

(4) Ortega, S.; Ibáñez, M.; Liu, Y.; Zhang, Y.; Kovalenko, M. V.; Cadavid, D.; Cabot, A. Bottom-up engineering of thermoelectric nanomaterials and devices from solution-processed nanoparticle building blocks. *Chem. Soc. Rev.* **2017**, *46*, 3510-3528.

(5) Heuer-Jungemann, A.; Feliu, N.; Bakaimi, I.; Hamaly, M.; Alkilany, A.; Chakraborty, I.; Masood, A.; Casula, M. F.; Kostopoulou, A.; Oh, E.; et al. The Role of Ligands in the Chemical Synthesis and Applications of Inorganic Nanoparticles. *Chem. Rev.* **2019**, *119*, 4819-4880.

(6) Shen, H.; Wu, Q.; Asre Hazer, M. S.; Tang, X.; Han, Y.-Z.; Qin, R.; Ma, C.; Malola, S.; Teo, B. K.; Häkkinen, H.; et al. Regioselective hydrogenation of alkenes over atomically dispersed Pd sites on NHC-stabilized bimetallic nanoclusters. *Chem* **2022**, doi.org/10.1016/j.chempr.2022.04.017.

(7) Wu, Z.; Zhang, S.; Liu, Z.; Mu, E.; Hu, Z. Thermoelectric converter: Strategies from materials to device application. *Nano Energy* **2022**, *91*, 106692.

(8) Zhang, Q.; Deng, K.; Wilkens, L.; Reith, H.; Nielsch, K. Micro-thermoelectric devices. *Nat. Electron.* **2022**, *5*, 333-347.

(9) Tan, G.; Zhao, L. D.; Kanatzidis, M. G. Rationally Designing High-Performance Bulk Thermoelectric Materials. *Chem. Rev.* **2016**, *116*, 12123-12149.

(10) Finefrock, S. W.; Yang, H.; Fang, H.; Wu, Y. Thermoelectric Properties of Solution Synthesized Nanostructured Materials. *Annu. Rev. Chem. Biomol. Eng.* **2015**, *6*, 247-266.

(11) Park, K.; Son, J. S.; Woo, S. I.; Shin, K.; Oh, M.-W.; Park, S.-D.; Hyeon, T. Colloidal synthesis and thermoelectric properties of La-doped $SrTiO_3$ nanoparticles. *J. Mater. Chem. A* **2014**, *2*, 4217-4224.

(12) Ibáñez, M.; Cadavid, D.; Zamani, R.; García-Castelló, N.; Izquierdo-Roca, V.; Li, W.; Fairbrother, A.; Prades, J. D.; Shavel, A.; Arbiol, J.; et al. Composition Control and Thermoelectric Properties of Quaternary Chalcogenide Nanocrystals: The Case of Stannite $Cu_2CdSnSe_4$. *Chem. Mater.* **2012**, *24*, 562-570.

(13) Ibanez, M.; Luo, Z.; Genc, A.; Piveteau, L.; Ortega, S.; Cadavid, D.; Dobrozhan, O.; Liu, Y.; Nachtegaal, M.; Zebarjadi, M.; et al. High-performance thermoelectric nanocomposites from nanocrystal building blocks. *Nat. Commun.* **2016**, *7*, 10766.

(14) Yazdani, S.; Pettes, M. T. Nanoscale self-assembly of thermoelectric materials: a review of chemistry-based approaches. *Nanotechnology* **2018**, *29*, 432001.

(15) Fan, F. J.; Wang, Y. X.; Liu, X. J.; Wu, L.; Yu, S. H. Large-scale colloidal synthesis of non-stoichiometric $Cu_2ZnSnSe_4$ nanocrystals for thermoelectric applications. *Adv. Mater.* **2012**, *24*, 6158-6163.

(16) Song, J. M.; Liu, Y.; Niu, H. L.; Mao, C. J.; Cheng, L. J.; Zhang, S. Y.; Shen, Y. H. Hot-injection synthesis and characterization of monodispersed ternary Cu_2SnSe_3 nanocrystals for thermoelectric applications. *J. Alloys Compd. and Compounds* **2013**, *581*, 646-652.

(17) Scheele, M.; Oeschler, N.; Meier, K.; Kornowski, A.; Klinke, C.; Weller, H. Synthesis and Thermoelectric Characterization of Bi_2Te_3 Nanoparticles. *Adv. Funct. Mater.* **2009**, *19*, 3476-3483.

(18) Fan, F. J.; Yu, B.; Wang, Y. X.; Zhu, Y. L.; Liu, X. J.; Yu, S. H.; Ren, Z. Colloidal synthesis of $Cu_2CdSnSe_4$ nanocrystals and hot-pressing to enhance the thermoelectric figure-of-merit. *J. Am. Chem. Soc.* **2011**, *133*, 15910-15913.

(19) Zhang, A.; Zhang, B.; Lu, W.; Xie, D.; Ou, H.; Han, X.; Dai, J.; Lu, X.; Han, G.; Wang, G.; et al. Twin Engineering in Solution-Synthesized Nonstoichiometric Cu_5FeS_4 Icosahedral Nanoparticles for Enhanced Thermoelectric Performance. *Adv. Funct. Mater.* **2018**, *28*, 1705117.

(20) Ibáñez, M.; Zamani, R.; Li, W.; Cadavid, D.; Gorsse, S.; Katcho, N. A.; Shavel, A.; López, A. M.; Morante, J. R.; Arbiol, J.; et al. Crystallographic Control at the Nanoscale To Enhance Functionality: Polytypic Cu_2GeSe_3 Nanoparticles as Thermoelectric Materials. *Chem. Mater.* **2012**, *24*, 4615-4622.

(21) Cadavid, D.; Ibáñez, M.; Shavel, A.; Durá, O. J.; López De La Torre, M. A.; Cabot, A. Organic ligand displacement by metal salts to enhance nanoparticle functionality: thermoelectric properties of Ag_2Te. *J. Mater. Chem. A* **2013**, *1*, 4864.

(22) Ibáñez, M.; Korkosz, R. J.; Luo, Z.; Riba, P.; Cadavid, D.; Ortega, S.; Cabot, A.; Kanatzidis, M. G. Electron Doping in Bottom-Up Engineered Thermoelectric Nanomaterials through HCl-Mediated Ligand Displacement. *J. Am. Chem. Soc.* **2015**, *137*, 4046-4049.

(23) Ibáñez, M.; Hasler, R.; Genç, A.; Liu, Y.; Kuster, B.; Schuster, M.; Dobrozhan, O.; Cadavid, D.; Arbiol, J.; Cabot, A.; et al. Ligand-Mediated Band Engineering in Bottom-Up Assembled SnTe Nanocomposites for Thermoelectric Energy Conversion. *J. Am. Chem. Soc.* **2019**, *141*, 8025-8029.

(24) Karthikeyan, V.; Oo, S. L.; Surjadi, J. U.; Li, X.; Theja, V. C. S.; Kannan, V.; Lau, S. C.; Lu, Y.; Lam, K.-H.; Roy, V. A. L. Defect Engineering Boosted Ultrahigh Thermoelectric Power Conversion Efficiency in Polycrystalline SnSe. *ACS Appl. Mater. Interfaces* **2021**, *13*, 58701-58711.

(25) Ludemann, M.; Gordan, O. D.; Zahn, D. R. T.; Beekman, M.; Atkins, R.; Johnson, D. C. Raman Spectroscopy Insights into the Size-Induced Structural Transformation in SnSe Nanolayers. *Langmuir* **2014**, *30*, 8209-8214.

(26) Wang, K.; Zhao, N.; Lei, S.; Yan, R.; Tian, X.; Wang, J.; Song, Y.; Xu, D.; Guo, Q.; Liu, L. Promising biomass-based activated carbons derived from willow catkins for high performance supercapacitors. *Electrochim. Acta* **2015**, *166*, 1-11.

(27) Sevilla, M.; Fuertes, A. B. Direct Synthesis of Highly Porous Interconnected Carbon Nanosheets and Their Application as High-Performance Supercapacitors. *ACS Nano* **2014**, *8*, 5069-5078.

(28) Xu, H.; She, X.; Fei, T.; Song, Y.; Liu, D.; Li, H.; Yang, X.; Yang, J.; Li, H.; Song, L.; et al. Metal-Oxide-Mediated Subtractive Manufacturing of Two-Dimensional Carbon Nitride for High-Efficiency and High-Yield Photocatalytic H_2 Evolution. *ACS Nano* **2019**, *13*, 11294-11302.

(29) Wang, W.; Shang, L.; Chang, G.; Yan, C.; Shi, R.; Zhao, Y.; Waterhouse, G. I. N.; Yang, D.; Zhang, T. Intrinsic Carbon-Defect-Driven Electrocatalytic Reduction of Carbon Dioxide. *Adv. Mater.* **2019**, *31*, e1808276.

(30) Liu, D.; Wu, C.; Chen, S.; Ding, S.; Xie, Y.; Wang, C.; Wang, T.; Haleem, Y. A.; ur Rehman, Z.; Sang, Y.; et al. In situ trapped high-density single metal atoms within graphene: Iron-containing hybrids as representatives for efficient oxygen reduction. *Nano Res.* **2018**, *11*, 2217-2228.

(31) Ye, X.; Lin, Z.; Liang, S.; Huang, X.; Qiu, X.; Qiu, Y.; Liu, X.; Xie, D.; Deng, H.; Xiong, X.; et al. Upcycling of Electroplating Sludge into Ultrafine Sn@C Nanorods with Highly Stable Lithium Storage Performance. *Nano Lett.* **2019**, *19*, 1860-1866.

(32) Duan, Y.; Du, S.; Tao, H.; Yang, X. Sn@C composite for lithium ion batteries: amorphous vs. crystalline structures. *Ionics* **2021**, *27*, 1403-1412.

(33) Lin, Y.; Yang, L.; Zhang, Y.; Jiang, H.; Xiao, Z.; Wu, C.; Zhang, G.; Jiang, J.; Song, L. Defective Carbon-CoP Nanoparticles Hybrids with Interfacial Charges Polarization for Efficient Bifunctional Oxygen Electrocatalysis. *Adv. Energy Mater.* **2018**, *8*, 1703623.

(34) Chang, X.; Wang, T.; Liu, Z.; Zheng, X.; Zheng, J.; Li, X. Ultrafine Sn nanocrystals in a hierarchically porous N-doped carbon for lithium-ion batteries. *Nano Res.* **2017**, *10*, 1950-1958.

(35) Snyder, G. J.; Toberer, E. S. Complex thermoelectric materials. *Nat. Mater.* **2008**, *7*, 105-114.

(36) Wirtz, L.; Rubio, A. The phonon dispersion of graphite revisited. *Solid State Commun.* **2004**, *131*, 141-152.

(37) Sosso, G. C.; Deringer, V. L.; Elliott, S. R.; Csányi, G. Understanding the thermal properties of amorphous solids using machine-learning-based interatomic potentials. *Mol. Simul.* **2018**, *44*, 866-880.

(38) Mansour, B. A.; Tahoon, K. H.; El-Sharkawy, A. A. Thermophysical properties and mechanism of heat transfer of non-stoichiometric $Cu_{2-x}S$. *Phys. Status Solidi A* **1995**, *148*, 423-430.

(39) Bullen, A. J.; O'Hara, K. E.; Cahill, D. G.; Monteiro, O.; Von Keudell, A. Thermal conductivity of amorphous carbon thin films. *J. Appl. Phys.* **2000**, *88*, 6317-6320.

(40) Kakodkar, R. R.; Feser, J. P. Probing the validity of the diffuse mismatch model for phonons using atomistic simulations. *Phys. Rev. B* **2017**, *95*, 125434.

(41) Anstis, G. R.; Chantikul, P.; Lawn, B. R.; Marshall, D. B. A Critical Evaluation of Indentation Techniques for Measuring Fracture Toughness: I, Direct Crack Measurements. *J. Am. Ceram. Soc.* **1981**, *6*, 533-538.

(42) Drory, M. D.; Ager, J. W.; Suski, T.; Grzegory, I.; Porowski, S. Hardness and fracture toughness of bulk single crystal gallium nitride. *Appl. Phys. Lett.* **1996**, *6*, 4044-4046

(43) Jiang, B.; Liu, X.; Wang, Q.; Cui, J.; Jia, B.; Zhu, Y.; Feng, J.; Qiu, Y.; Gu, M.; Ge, Z.; et al. Realizing high-efficiency power generation in low-cost PbS-based thermoelectric materials. *Energy Environ. Sci.* **2020**, *13*, 579-591.